Desalination and Water Treatment
www.deswater.com

doi: 10.5004/dwt.2023.30110

314 (2023) 263–275
December

Photo-assisted assembly of MgO/Fe_2O_3 composites for photocatalytic Rhodamine B degradation and their mimicking activity

Manojkumar Utaiyachandran[a], Kaliannan Durairaj[b], Alagarasan Jagadeesh Kumar[c], Subpiramaniyam Sivakumar[d,*], Velmurugan Palanivel[e], Palaninaicker Senthilkumar[a,*]

[a]*Department of Environmental Science, School of Energy & Environmental Sciences, Periyar University, Salem, Tamil Nadu 636011, India, emails: pskumares@periyaruniversity.ac.in (P. Senthilkumar), utaiyachandran@gmail.com (M. Utaiyachandran)*
[b]*Department of Infection Biology, School of Medicine, Wonkwang University, Iksan 54538, South Korea, email: kmdurairaj@gmail.com*
[c]*School of Chemical Engineering, Yeungnam University, Gyeongsan-si, 712-749, South Korea, email: jaga.jagadeesh@gmail.com*
[d]*Department of Bioenvironmental Energy, College of Natural Resource and Life Sciences, Pusan National University, Miryang-si, Gyeongsangnam-do 50463, Republic of Korea, email: ssivaphd@yahoo.com*
[e]*Centre for Materials Engineering and Regenerative Medicine, Bharath Institute of Higher Education and Research, Selaiyur, Chennai, Tamil Nadu 600126, India, email: palanivelmurugan2008@gmail.com*

Received 3 July 2023; Accepted 1 November 2023

ABSTRACT

In this study, MgO/Fe_2O_3 composites were synthesized from *Annona squamosa* seed extracts via a photo-assisted method using sunlight (S_1), sodium (S_2), and light emitting diode (LED) (S_3) light sources. The three MgO/Fe_2O_3 composites were characterized using different techniques. X-ray diffraction patterns revealed the crystalline nature of the composites, and Fourier-transform infrared spectroscopy revealed 425 and 586 cm^{-1} stretching, indicating Mg–O and Fe–O bond formation, respectively. Scanning electron microscopy results revealed that the composites had diverse sizes and shapes. Moreover, the UV-Visible diffuse reflectance spectra showed that the bandgaps for S_1, S_2 and S_3 were 3.03, 3.10, and 3.03 eV, respectively. Dynamic light scattering results showed that the surface charges for S_1, S_2, and S_3 were −30.5, −28, and −24.9 mV, respectively. The photocatalytic Rhodamine B degradation efficiency of the MgO/Fe_2O_3 composites was examined in batch mode. The reaction rate constants (k) for S_1, S_2, and S_3 composites were 0.02919, 0.02769, and 0.02813 min^{-1}, respectively, indicating that the reaction followed a pseudo-first-order kinetics model. The catalytic efficiency of the MgO/Fe_2O_3 composites in a mimetic reaction revealed their effectiveness in the amine-to-imine conversion. Therefore, the MgO/Fe_2O_3 composites can be used for industrial wastewater remediation and medical applications.

Keywords: MgO/Fe_2O_3 composites; Rhodamine B; High-performance liquid chromatography; Pseudo-first-order kinetics; Mimicking activity

1. Introduction

Rhodamine B (RhB) is a cationic fluorescent dye that is widely used as a colorant in the textile, food, cosmetic, and pharmaceutical industries [1]. Wastewater contaminated with RhB is often discharged untreated into the environment [2]. Because of its long-term persistence in aquatic ecosystems, RhB may threaten biological systems owing to its carcinogenic and neurotoxic effects [3]. Therefore, various remediation techniques such as adsorption [2], membrane filtration [4] electrochemical oxidation [5], electrocoagulation [6], advanced oxidation [7] and sono-chemical degradation [8] are used to remove RhB from wastewater.

However, currently used methods have notable disadvantages. Adsorption cannot be used commercially because

* Corresponding authors.

of the lack of high-adsorbing molecules and commercial-scale columns. Although previously reported membrane filtration techniques have high efficacy for remediation with low space requirements, they are expensive [9]. The main drawbacks of electrochemical oxidation methods include the costs related to electrical supply, the low conductance of many wastewaters that necessitate electrolyte addition, activity loss, and reduced electrode lifetime owing to organic material deposition on the electrode surface [10]. The disadvantages of electrocoagulation include electrode passivation and high electricity consumption due to its low wastewater conductivity [11]. Moreover, electrocoagulation generates chemical sludge (secondary pollutants) that requires further treatment to achieve efficient sludge reduction [12]. The main drawbacks of advanced oxidation processes are their high cost owing to the use of expensive reagents (such as H_2O_2) and high energy consumption (for O_3 generation or UV irradiation) [13]. Finally, the sonochemical process has high energy requirements because of the large amount of electrical power necessary to remove pollutants, which increases costs and makes scaling-up challenging [14]. Therefore, because of their cost-effectiveness, sustainability, and eco-friendliness, composite-mediated photocatalysts have emerged as green strategies for photo-assisted RhB degradation [15].

Photocatalysts such as CuO/PVA [16], V_2O_5-rGO [17], $NaBH_4$-spiked ZnS [18], C_3N_4/Ag@$CoWO_4$ [19], CuO/ZnO [20], and $BiVO_4$/Fe_3O_4/rGO [21] have been used in various studies to degrade RhB in aqueous systems. Various methods, such as the sol–gel method, chemical reduction, coprecipitation, and hydrothermal synthesis, are used to synthesize nanomaterials; however, the chemicals used in these methods are harmful to the environment [22]. Therefore, synthesizing nanomaterials from plant extracts has recently gained attention, as it represents an eco-friendly and non-toxic approach [20].

Among the various nanomaterials, MgO nanoparticles have been widely used because of their catalytic properties, high thermal conductivity, high surface activity, high stability, biocompatibility, and a large number of surface-active sites [23]. In addition, Fe_2O_3 nanoparticles exhibit excellent catalytic and reductive properties that are beneficial for wastewater treatment [22]. *Annona squamosa* is a medicinal plant widely used in the pharmaceutical industry. The bark, root, leaf, stem fruit, peel, and seed extracts of *A. squamosa* can cure several diseases [3]; however, the seeds are non-edible and are typically discarded [24]. In this study, MgO/Fe_2O_3 composites were prepared by the photoirradiation of *A. squamosa* seed extracts. To the best of our knowledge, this is the first report describing the synthesis of MgO/Fe_2O_3 composites from *A. squamosa* seed extract, their use in the photodegradation of RhB, and their mimicking activities.

2. Materials and methods

2.1. Chemicals

Analytical grade (99.5%) magnesium sulfate heptahydrate ($MgSO_4{\cdot}7H_2O$), 99% ferric chloride ($FeCl_3$), 98% sodium hydroxide (NaOH), 37% hydrochloric acid (HCl), and 35% hydrogen peroxide (H_2O_2) were purchased from Loba Chemie Pvt., Ltd., (India) and used without further purification.

2.2. A. squamosa seed extract preparation

A. squamosa seeds were collected from Periyar University, India, dried under sunlight for 2 d, and ground to a powder. Subsequently, the seed powder (6 g) was poured into 200 mL of distilled water (DW) in a 500 mL Erlenmeyer flask and shaken at 120 rpm for 3 d at room temperature (27°C + 2°C). The solution was then filtered through Whatman Paper No. 42, and the filtrate was stored for nanoparticle synthesis.

2.3. Photo-assisted MgO and Fe_2O_3 nanoparticle synthesis

$MgSO_4$ (0.1 M) and $FeCl_3$ (0.02 M) were added to 50 mL of seed extract in a 500 mL beaker and irradiated for 6 h under a commercial sodium lamp (60 W) (Crompton Greaves, GLS60, India), a white light emitting diode (LED) lamp (9 W) (Philips, B22, India), and sunlight (10 am to 4 pm). Light bulbs were fitted to the top of a black box, and the distance from the beaker was adjusted to 10 cm. The beakers were stored in the dark for 18 h to prevent interference from external light. After 3 d, the solutions were dried at 70°C for 12 h in a hot-air oven and ground to a powder. The dried powder was annealed at 500°C for 3 h and then stored at room temperature.

2.4. MgO/Fe_2O_3 composite preparation

MgO/Fe_2O_3 composites were fabricated via ultrasonication to obtain the desired MgO:Fe_2O_3 ratio. MgO/Fe_2O_3 fabrication involved the individual weighing, mixing, and grinding of the three types of MgO and Fe_2O_3 nanoparticles. Subsequently, the mixed nanoparticles were dispersed in 50 mL DW and ultrasonicated for 30 min at 25°C, after which the sample was dried at 100°C for 24 h and stored.

2.5. RhB photocatalytic degradation

The photocatalytic activities of the prepared MgO/Fe_2O_3 composites against RhB were also evaluated. Briefly, 20 mg of the S_1, S_2, and S_3 composites were added separately to 250 mL beakers containing 50 mL of 20 ppm RhB, and three suspension reactor sets were combined to examine the efficiencies of the three photocatalysts. The samples were placed in the dark for 30 min to attain adsorption–desorption equilibrium, after which the solution mixture was irradiated with sunlight. After a specific period of solar irradiation, the photocatalyst was separated from the aqueous RhB solution by centrifugation at 10,000 rpm for 5 min. The effects of the nanoparticle ratio in the composite, pH, catalytic dose, dye concentration in the medium, and H_2O_2 concentration on RhB photodegradation were also evaluated. Photocatalytic RhB degradation was examined using a UV-Visible spectrophotometer and the percentage degradation was calculated [25]:

$$\text{Degradation}(\%) = \frac{A_0 - A}{A_0} \times 100 \quad (1)$$

where A_0 is the initial dye concentration and A is the dye concentration after solar irradiation.

2.6. MgO/Fe_2O_3 composites (1:2) characterization

The phase purity and crystalline nature of the composites was determined using an X-ray diffraction (XRD) spectrometer (Rigaku MiniFlex, Japan) with monochromatic Cu Kα radiation (λ_{Cu} = 1.54 Å) operating at 40 mA and 40 kV and a scanning range of 10°–80°. The functional groups were analyzed using a Fourier-transform infrared (FTIR) spectrophotometer (Bruker Tensor 27 Spectrophotometer, Germany) over 4,000–450 cm^{-1} with 4.0 cm^{-1} resolution. The morphology and distribution of the metallic elements were analyzed by scanning electron microscopy (SEM) energy-dispersive X-ray spectroscopy (EDX) mapping obtained using a 20 kV-operated EDX Inc., and the surface morphology and size were characterized using SEM (EVO 18, Carl Zeiss Microscopy GmbH, Germany). UV-Visible diffuse reflectance (UV-Vis DRS) was recorded at 200–800 nm using an Ocean Optics USB 4000 spectrometer (China), and the particle size (presented as diameter) and zeta potential were measured using dynamic light scattering (DLS) (Zetasizer, Malvern Instruments Ltd., UK). The particle size distribution was obtained from a graph of the particle size (hydrodynamic diameter of particles) and intensity percentage. A backscattering detector was used in this configuration. The zeta potential distribution was obtained from the graph of the zeta potential and total counts. The absorption spectra of the RhB solutions at 200–800 nm were obtained using a UV-Visible spectrophotometer (Shimadzu, 1800-Series, Japan) calibrated using DW (blank) and a quartz cuvette with a 1-cm path length as the sample holder.

2.7. High-performance liquid chromatography analysis

The samples were analyzed using high-performance liquid chromatography (HPLC) with a UV detector at 554 nm and an injector with a 20.0 µL loop. Chromatography was performed using a C18 reversed-phase column (150 mm × 4.6 mm I.D., 5 mm, Jasco Corporation, Japan) at room temperature. The mobile phase comprised 70:30 (v/v) methanol/water. The flow rate was set to 1.0 mL/min [26].

2.8. Mimicking activity

For the MgO/Fe_2O_3 composite-based redox reaction, 100 mg (0.001 M) of 2-aminophenol was dispersed in 40 mL of ethanol, and 5 mg of the composite was added at 30°C without using any oxidant. Subsequently, the samples were collected every 5 min, and the absorbance peak was measured by UV-Visible spectrophotometer. The percentage synthase activity was calculated using Eq. (2):

$$\text{Synthase activity}(\%) = \frac{A - A_0}{A} \times 100 \quad (2)$$

where A and A_o are the initial and final concentrations of the solution, respectively.

3. Results and discussion

3.1. XRD analysis of composites

Fig. 1 shows the XRD patterns of the synthesized MgO/Fe_2O_3 composites. All the diffraction peaks were relatively distinct, confirming the good crystallinity of all the composites. The weak-intensity peaks indicated the presence of MgO particles in the sample and were indexed to 37.2° (111), 42.4° (200), 62.2° (220), 74.2° (311), and 78.4° (222) (JCPDS, No. 87-0653). Subsequently, the Fe_2O_3 patterns at 2θ positions of 14.1°, 17.3°, 24.2°, 30.4°, 35.5°, 43.6°, and 65.2° were assigned to the *hkl* planes of (110), (111), (210), (220), (311), (400), and (220), respectively. The results were compared with the patterns of the Fe_2O_3 nanoparticles synthesized in previous studies (JCPDS 39-1346) [27]. The production of samples and the presence of mixed XRD peaks were observed and verified. The XRD pattern of MgO/Fe_2O_3 showed characteristic peaks of both MgO and Fe_2O_3, revealing the crystalline nature of the composites. The results showed that The Fe_2O_3 peaks were stronger than the MgO peaks owing to the high Fe_2O_3 concentration in the composites. During synthesis, light may favor the local heating of the precursor solution, thus accelerating the chemical reaction and increasing the nucleation efficiency. Despite the strongly forbidden nature of the corresponding electronic transitions, some photoexcited states of the complex precursor may have been oxidized by anions [28].

3.2. FTIR analysis

Fig. 2 shows the FTIR spectra of the photocatalyst surfaces from which the functional groups of the MgO/Fe_2O_3 composites were investigated. The peak at 3,454 cm^{-1} was attributed to the O–H stretching vibration of hydroxyl functional groups, including hydrogen bonding [29]. The stretching vibrations of hydroxyl groups on solid surfaces and those with terminal OH groups are characteristic of metal oxides [30]. Peaks around 1,650 cm^{-1} were attributed to the stretching vibration of aromatic C=C bond [29]. Additionally, the transmittance at 1,014 cm^{-1} indicated the presence of C–O stretching between 1,014 and 1,108 cm^{-1}, which might be due to the presence of covalent linking of

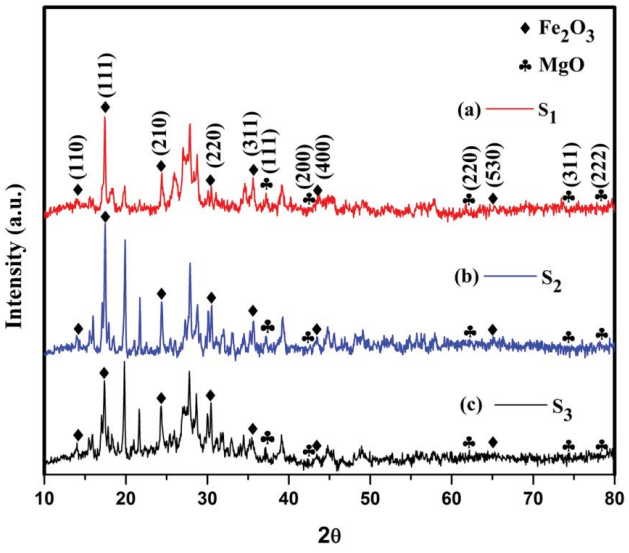

Fig. 1. X-ray diffraction analyses of MgO/Fe_2O_3 composites irradiated with (a) sunlight (S_1), (b) sodium lamp (S_2), and (c) LED (S_3).

ether or ester groups with nanoparticles [31]; the peaks at 425 cm^{-1} indicated the formation of the Mg–O bond [29]. The strong additional peak at 586 cm^{-1} was attributed to the stretching vibration of Fe–O present in MgO/Fe_2O_3 composites [32]. Previous reports have confirmed that several functional groups present in *A. squamosa* seed extract act as reducing and limiting agents in the synthesis of stable nanoparticles, and the above-mentioned infrared bands could indicate the presence of esters, ethers, carbonyl (polyol), or aromatic compounds.

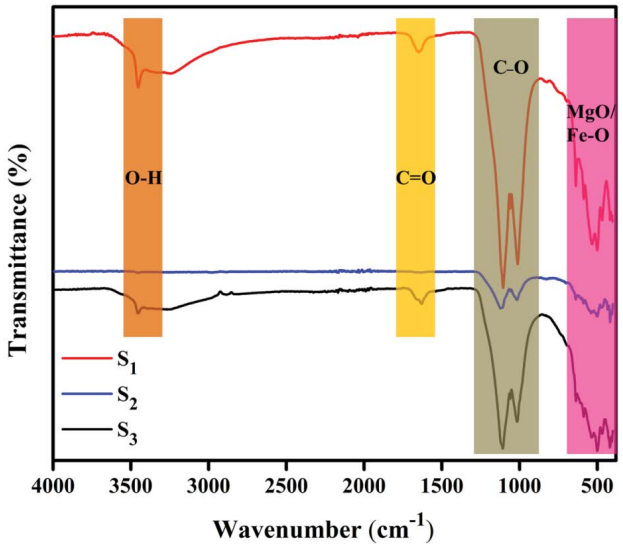

Fig. 2. Fourier-transform infrared spectroscopy analysis of MgO/Fe_2O_3 composites.

3.3. Scanning electron microscopy analysis

SEM was used to examine the surface morphologies of the MgO/Fe_2O_3 composites. The SEM images of the MgO/Fe_2O_3 composites at different magnifications show crystallite aggregations of diverse sizes and shapes (Fig. 3a–i). These images, combined with EDX, were used to identify and quantify the particles in the composites. The EDX spectrum of S_1 composite showed that the quantities of Mg, Fe, O, and C were 3.24, 14.06, 40.19, and 29.26, respectively. The EDX spectrum of the S_2 composite showed an elemental composition, with the weight percentages of Mg, Fe, O, and C being 2.97, 14.89, 37.96, and 30.87, respectively (Fig. 4a and b). Fig. 4c shows the elemental composition of the S_2 composite, with weight percentages of Mg, Fe, O, and C of 3.84, 13.30, 39.25, and 30.48, respectively. An additional sulfur-related peak was observed in this spectrum of the *A. squamosa* seed extract, which contains sulfone and sulfate esters [33]. The EDX spectrum of the MgO/Fe_2O_3 composites shows elemental peaks for Mg, Fe, O, and C (Fig. 4c), indicating the purity of the synthesized composites.

3.4. Optical analysis

Fig. 5 shows the UV-Vis absorption spectra and forbidden bandwidths of the prepared MgO/Fe_2O_3 composites. All the three composites showed absorption bands in both the UV and visible regions, indicating that these photocatalysts could be excited by a wide spectrum of light. The light absorption capacities of the synthesized samples were examined by UV-DRS, and the resulting spectral properties are shown in Fig. 5. The optical bandgap values of the synthesized MgO/Fe_2O_3 composites were calculated using the Tauc method [Eq. (3)] [34]:

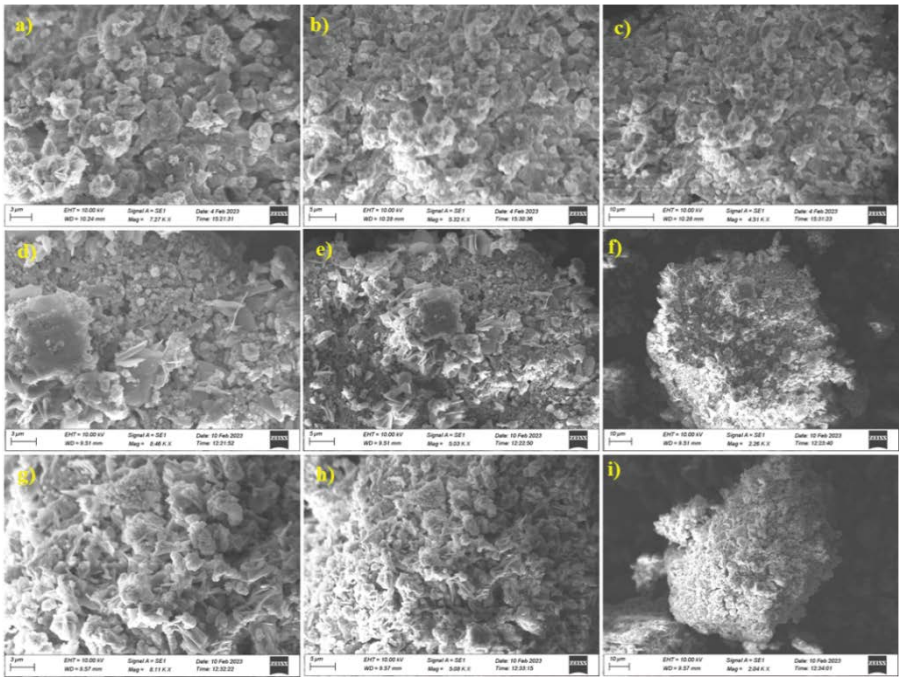

Fig. 3. Scanning electron microscopy analysis of MgO/Fe_2O_3 composites irradiated with (a–c) sunlight (S_1), (d–f) sodium lamp (S_2), and (g–i) LED (S_3).

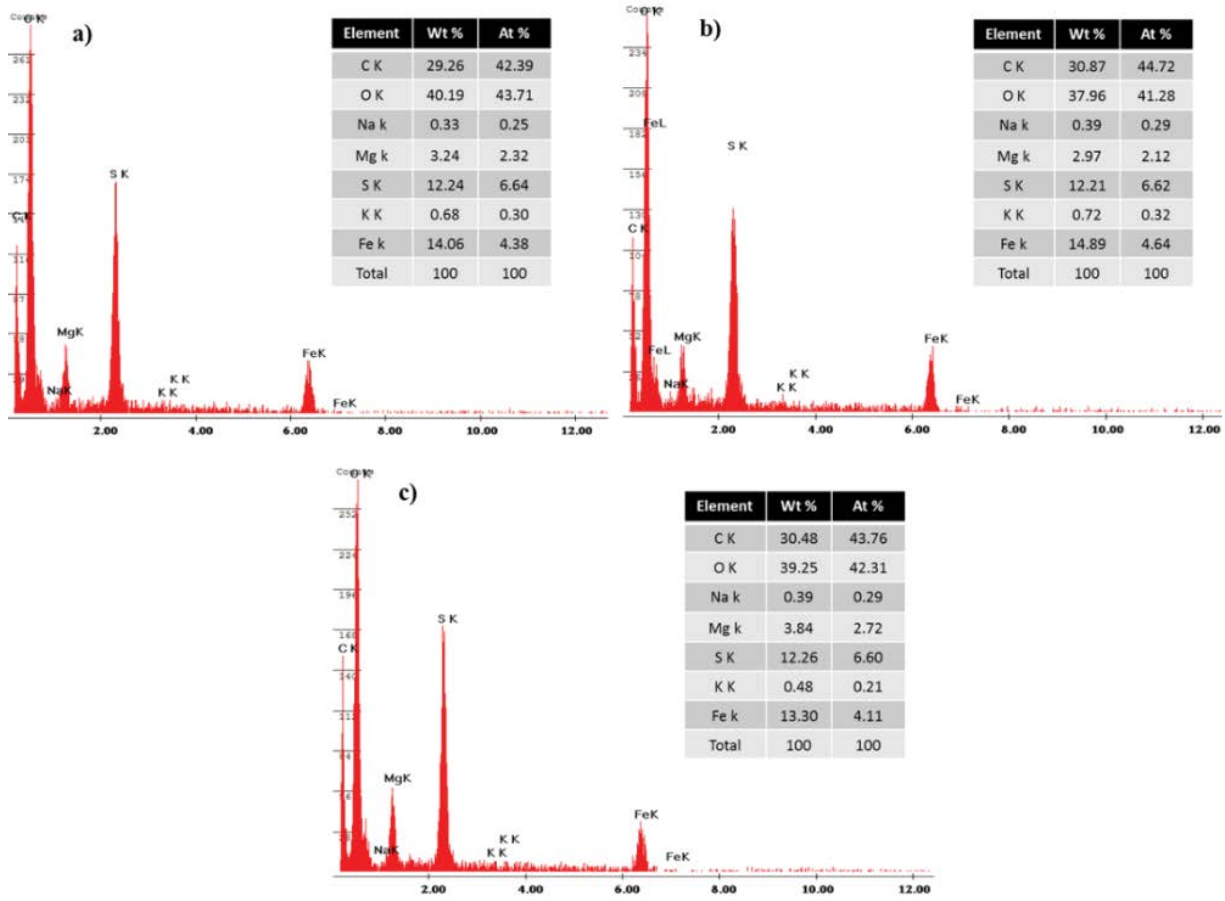

Fig. 4. Energy-dispersive X-ray spectra of MgO/Fe_2O_3 composites irradiated with (a) sunlight (S_1), b) sodium lamp (S_2), and c) LED (S_3).

$$\alpha h\nu = A\left(h\nu - E_g\right)^n \tag{3}$$

where α, h, υ, A, and E_g represent the extinction coefficient proportional to $F(R)$, Planck's constant (J/s), light frequency (s^{-1}), proportionality constant, and optical band gap of the material (eV), respectively. The value of the exponent n indicates the nature of the electronic transition between the valence and conduction bands of the semiconductors. The explored bandgaps of S_1, S_2, and S_3 were 3.03, 3.10, and 3.03 eV, respectively (Fig. 5b–d). The obtained bandgaps lie in the visible spectrum, confirming that the synthesized composites are suitable for photocatalytic dye degradation under sunlight. According to previous reports, the average bandgaps of MgO and Fe_2O_3 are greater than 4 and 2 eV, respectively [35,36]; however, we detected an intermediate bandgap, confirming MgO/Fe_2O_3 composite formation.

3.5. DLS analysis

The synthesized MgO/Fe_2O_3 composite (3 mg) was dispersed in DW (15 mL) and sonicated for 30 min. The zeta potentials and particle size distributions of the solutions were analyzed at room temperature (Fig. 6). DLS analysis revealed that the average S_1, S_2, and S_3 composite size was 739.2, 758.5, and 473.1 nm, respectively (Fig. 6a–c). The polydisperse index (PDI) of the S_1, S_2, and S_3 composite suspensions were 0.563, 0.645, and 0.435, respectively, indicating that the synthesized particles were of variable sizes and showed little agglomeration, which may be explained by the capping of the composites by some biomolecules [37]. A PDI > 0.7 indicates that the nano-dispersion has a wide size distribution and may not be suitable for DLS analysis. A PDI closer to 0.7 indicates that the polydisperse system has a higher tendency to aggregate than the monodisperse system [38].

The zeta potentials of the prepared S_1, S_2, and S_3 composites were −30.5, −28, and −24.9 mV, respectively (Fig. 6d–f). The results showed a less negative value than −35 mV, indicating that the synthesized material was moderately stable [39]. This is because when the zeta potential was negative, the nanoparticle surfaces were positively and negatively charged by MgO and Fe_2O_3, respectively [40,41]. Thus, the positively charged particles adsorbed the anions in the buffer and stabilized them. This was also evident in the particle size distribution analysis because of the nanoparticle agglomeration [39].

3.6. Effect of different nanoparticle ratios in composites for RhB degradation

The synthesized MgO and Fe_2O_3 nanoparticles were mixed in three MgO:Fe_2O_3 ratios (2:1, 1:1, and 1:2), and the

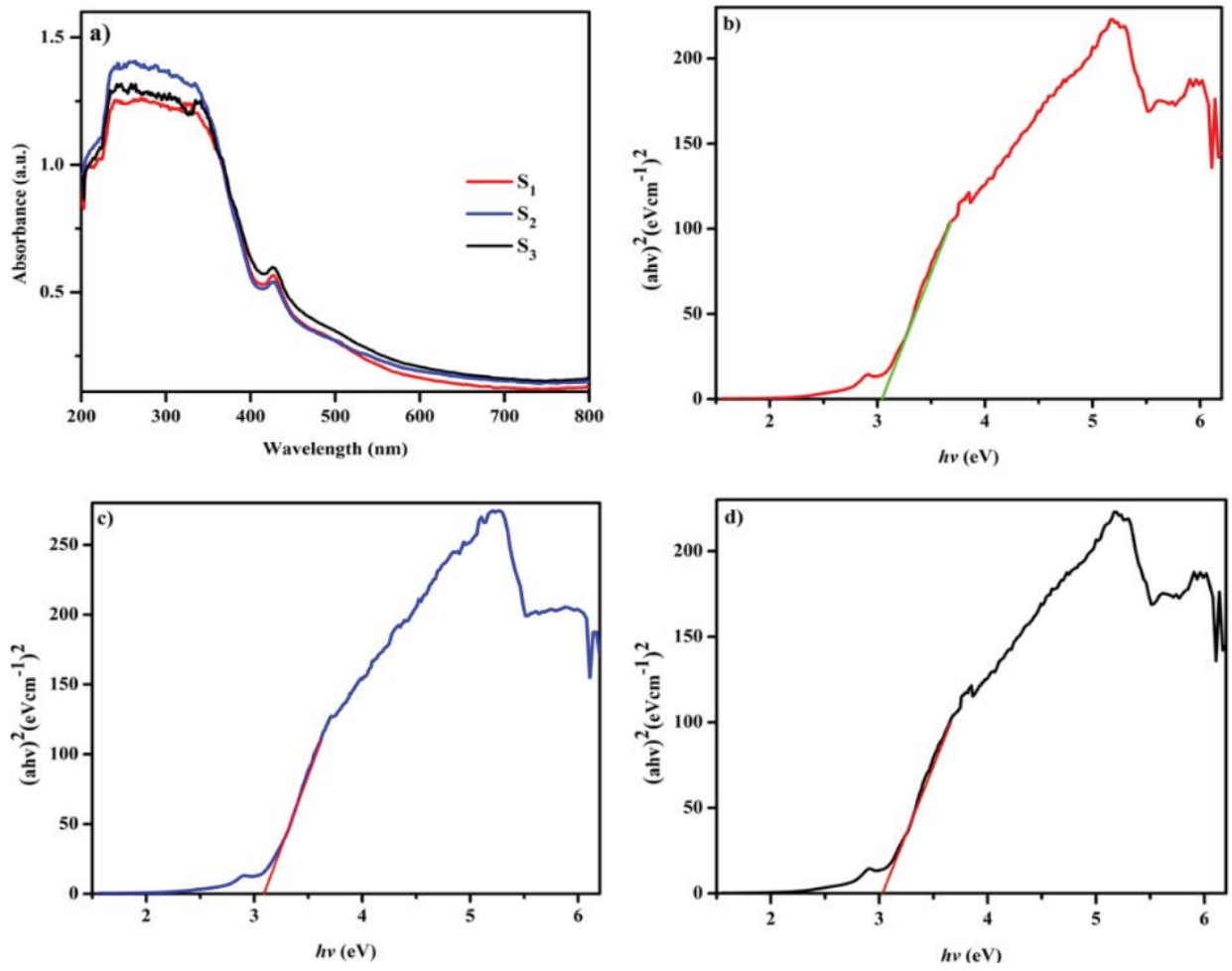

Fig. 5. (a) UV-Visible absorption spectrum of MgO/Fe_2O_3 and Tauc plot of (b) sunlight (S_1), (c) sodium lamp (S_2), and (d) LED (S_3) irradiated composites using Tauc plots.

catalyst efficiencies (20 mg) at different ratios under solar irradiation for 150 min were studied. After solar irradiation, the control solution (without the catalyst) exhibited negligible degradation (Fig. 7), demonstrating that RhB was not effectively degraded by direct photolysis. The degradation efficiencies of 2:1, 1:1, and 1:2 of S_1 were 84.53%, 97.63%, and 98.41%, respectively (Fig. 7a). The degradation efficiencies of 2:1, 1:1, and 1:2 S_2 were 88.77%, 95.38%, and 97.78%, respectively (Fig. 7b). The degradation efficiencies of 2:1, 1:1, and 1:2 of S_3 were 67.22%, 89.88%, and 95.53%, respectively (Fig. 7c). Therefore, the degradation efficiency increased with increasing Fe_2O_3 concentration in the composite.

3.7. Influence of pH on RhB removal

The pH of a solution is an important factor in photocatalytic processes. To study the impact of pH on the photodegradation efficiency, experiments were performed at pH 4, 7, and 10 with an initial dye concentration of 20 ppm, 20 mg of photocatalyst, and 150 min of solar irradiation (Fig. 8). The photocatalytic RhB degradation efficiencies of the S_1 composite at pH 4, 7, and 10 were 93.05%, 88.49%, and 43.80%, respectively (Fig. 8a). The dye degradation efficiencies of the S_2 composite at pH values of 4, 7, and 10 were 93.05%, 89.89%, and 63.91%, respectively (Fig. 8b). The dye degradation efficiencies of the S_3 composite at pH values of 4, 7, and 10 were 90.66%, 89.48%, and 38.11%, respectively (Fig. 8c). Thus, increasing the pH from 4.0 to 7.0 gradually decreased the photocatalytic degradation efficiency, followed by a steep decrease at pH 10. The experimental results showed that the degradation efficiency was higher in acidic media than in neutral or alkaline media. The photocatalyst surface was negatively charged (Fig. 6d–f), and RhB was slightly positively charged at this pH, leading to stronger interactions between the two components. However, at high pH, both the photocatalyst surface and RhB were negatively charged, leading to the repulsive behavior of the photocatalyst towards RhB. These results indicate that an acidic medium favors RhB degradation [42].

3.8. Effect of photocatalyst dose on RhB degradation

The optimum photocatalyst dose for RhB degradation was determined to avoid the use of excess catalyst. The dose changed the surface area of the catalyst, which is an important factor for dye degradation. The photocatalytic

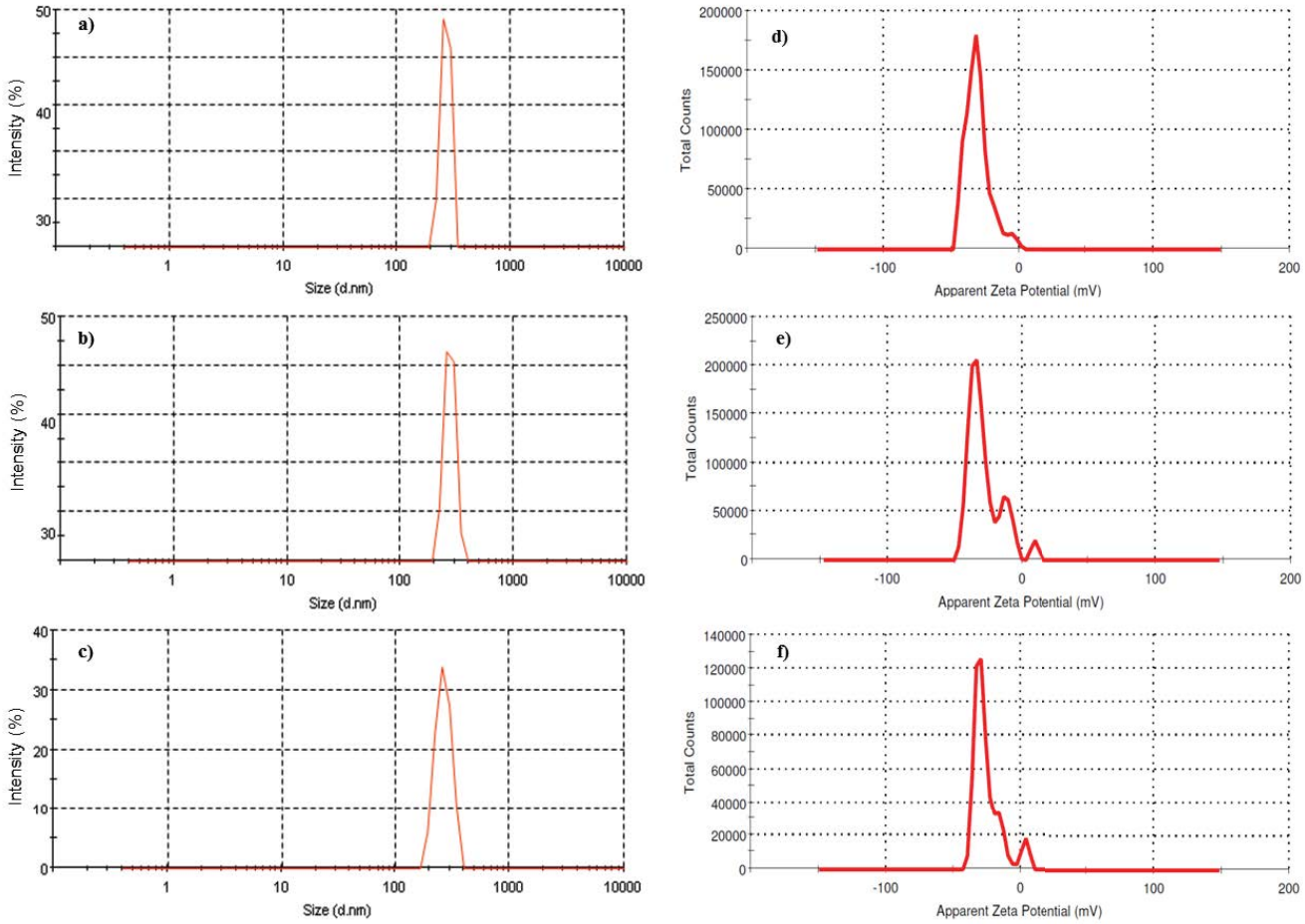

Fig. 6. Dynamic light scattering spectrum of MgO/Fe_2O_3 composite. (a–c) Particle-size distribution and (d–f) zeta potential of composites irradiated with sunlight (S_1), sodium lamp (S_2), and LED (S_3).

efficiency of 10–40 mg of each composite was evaluated under solar irradiation for 150 min. Additionally, when the dye solution was irradiated with sunlight without a photocatalyst, the RhB degradation was less than 10%, indicating that solar irradiation was not the principal factor in RhB degradation. The photocatalytic RhB degradation efficiencies of 10, 20, 30, and 40 mg S_1 were 95.13%, 98.08%, 98.70%, and 98.41%, respectively (Fig. 9a); those of 10, 20, 30, and 40 mg S_2 were 96.68%, 97.64%, 98.67%, and 98.04%, respectively (Fig. 9b); and those of 10, 20, 30, and 40 mg S_3 were 97.38%, 97.89%, 98.23%, and 95.79%, respectively (Fig. 9c). These findings show that the optimal photocatalyst dose for all suspension reactors was 20 mg. The photodegradation efficiency increased with increasing photocatalyst dose owing to the availability of more active sites for dye degradation [34]; however, 40 mg of the catalyst reduced the efficiency of the degradation process. This can be attributed to increased agglomeration and a decreased number of active sites on the catalyst surface. The reduction of active sites affects photon adsorption to generate electrons and holes, which decreases light passage through the solution owing to turbidity and increases suspension opacity and light scattering.

3.9. Effect of initial RhB concentration on photocatalytic degradation

More than 90% of the RhB (20 ppm) was removed using the MgO/Fe_2O_3 composite within 150 min of solar light irradiation; therefore, the photocatalytic activity was tested using 10–40 ppm RhB. The photocatalyst (20 mg) and solution were placed under solar irradiation. The impact of dye concentration on the photocatalysts is shown in Fig. 10. The photocatalytic degradation efficiencies of 10, 20, 30, and 40 ppm of RhB with S_1 were 99.07%, 98.03%, 85.07%, and 46.06%, respectively. The photocatalytic degradation efficiencies of 10, 20, 30, and 40 ppm RhB with S_2 were 99.36%, 97.03%, 87.08%, and 55.89%, respectively. The photocatalytic degradation efficiencies of 10, 20, 30, and 40 ppm RhB with S_3 were 99.12, 97.32, 83.54, and 23.59%, respectively. The results showed that photocatalytic degradation efficiency decreased with increasing dye concentration. This may be because an increasing number of dye molecules were adsorbed on the photocatalyst surface with increasing initial dye concentration. In this case, adsorption on the photocatalyst surface decreases because many active sites are occupied by the dye molecules, consequently decreasing the generation of hydroxyl radicals (•OH) [43]. Furthermore,

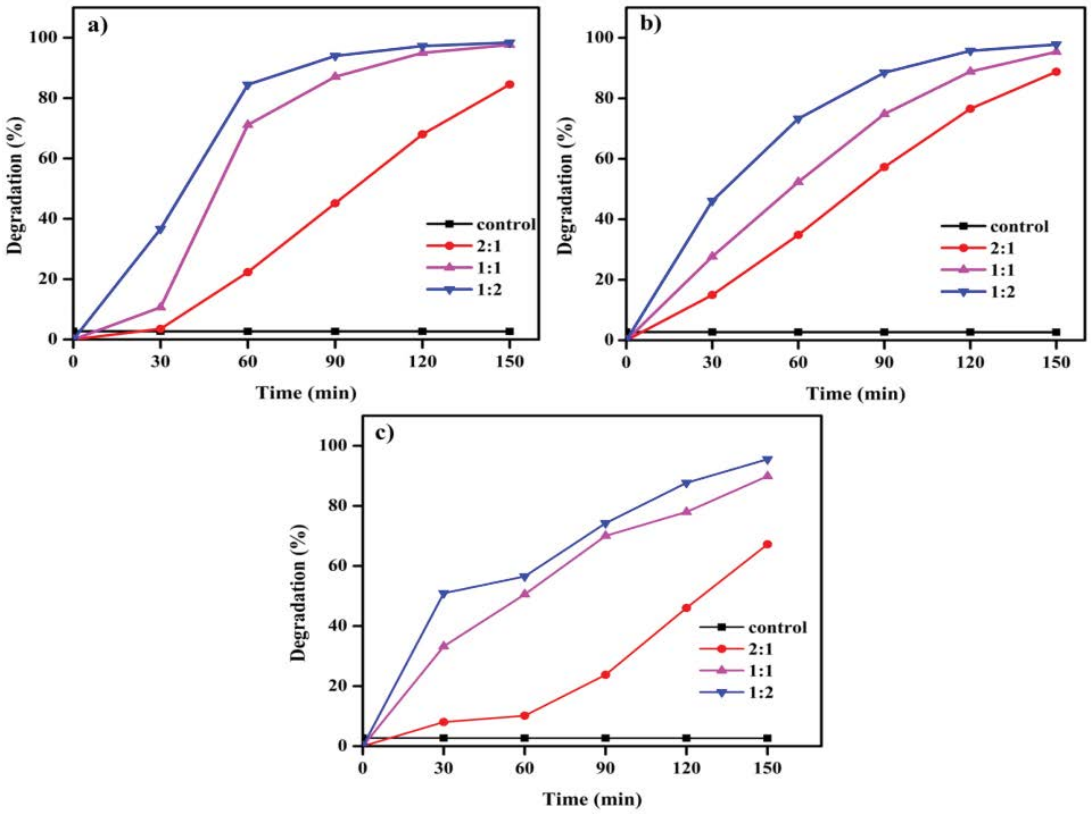

Fig. 7. Effect of different nanoparticle ratios on RhB degradation under solar irradiation by (a) sunlight (S_1), (b) sodium lamp (S_2), and (c) LED (S_3) composites.

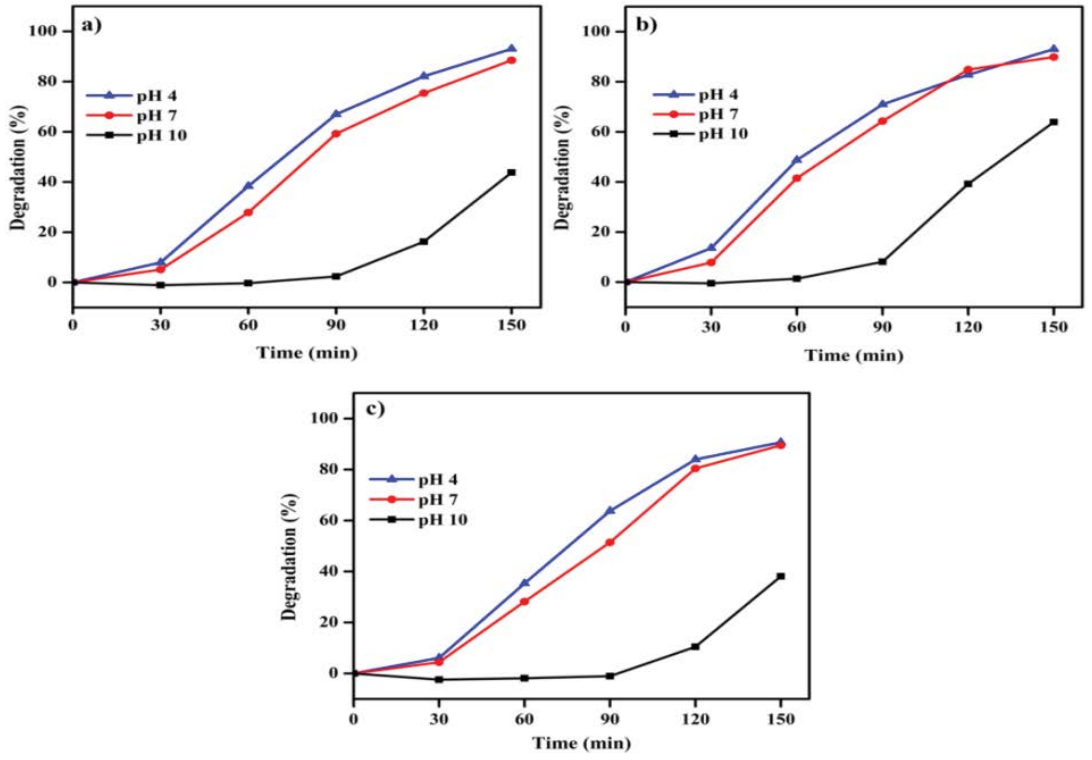

Fig. 8. Impact of initial pH on RhB degradation by (a) sunlight (S_1)-, (b) sodium lamp (S_2)-, and (c) LED (S_3)-irradiated composites.

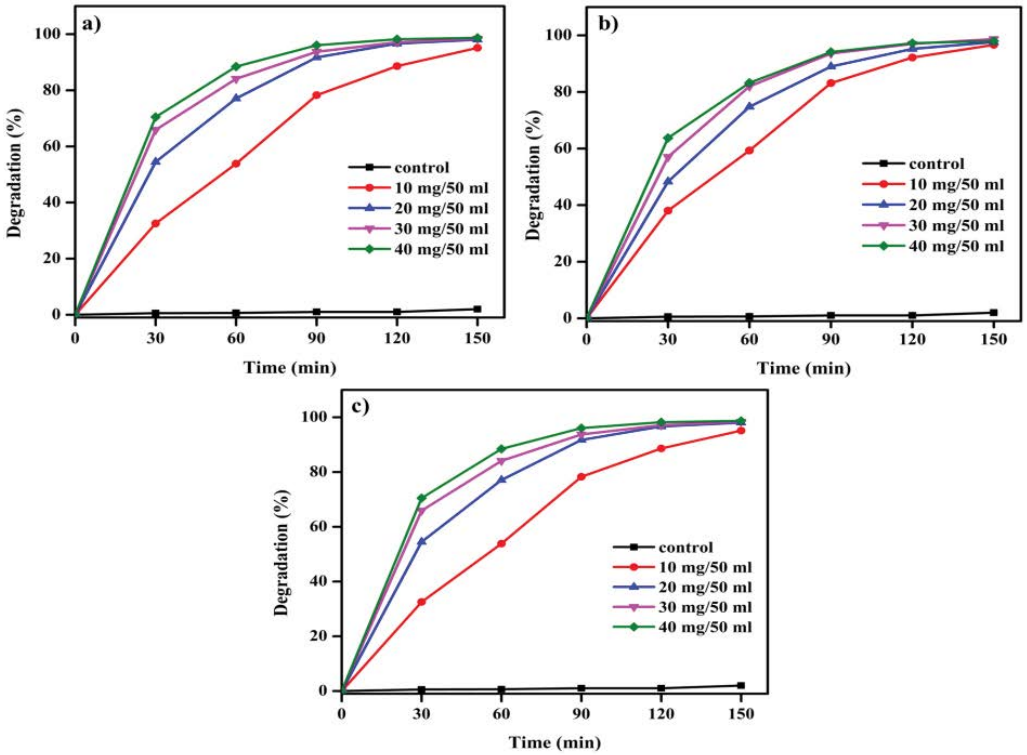

Fig. 9. Effect of catalyst dose on RhB degradation by (a) sunlight (S_1)-, (b) sodium lamp (S_2)-, and (c) LED (S_3)-irradiated composites.

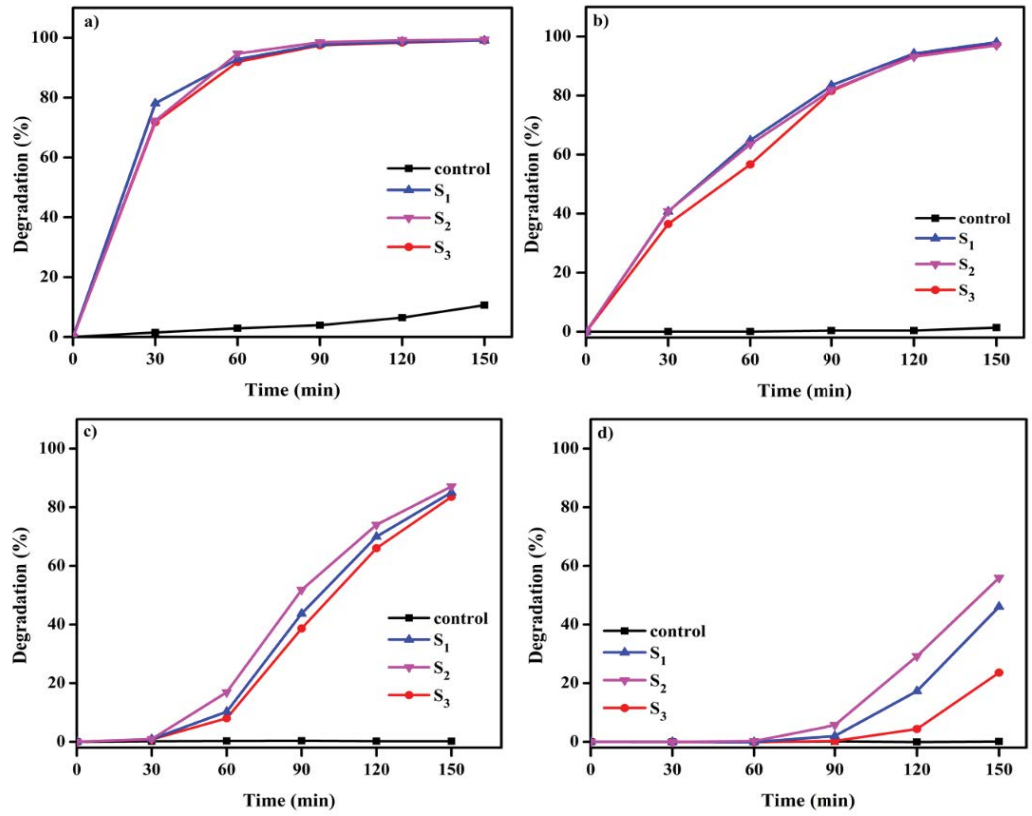

Fig. 10. Initial dye concentration impact on RhB degradation (a) 10, (b) 20, (c) 30 and (d) 40 ppm (S_1, S_2 and S_3 represent sunlight-, sodium lamp-, and LED-irradiated catalysis, respectively).

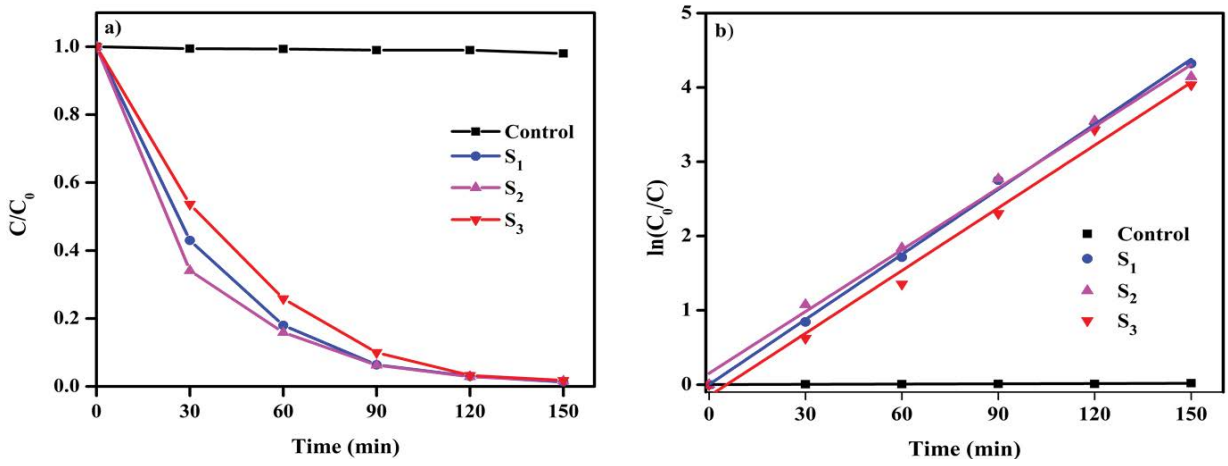

Fig. 11. (a) RhB photocatalytic degradation as a function of sunlight irradiation time for different composites and (b) plots of $\ln(C_0/C)$ vs. time of RhB degradation.

the degradation rate decreases at high dye concentrations because the solution becomes intensely colored and the path length of the photons entering the solution decreases, thus limiting the number of photons absorbed by the photocatalyst surface [44].

3.10. RhB degradation kinetic studies of MgO/Fe_2O_3 composites

Fig. 11 shows the RhB degradation kinetics curves of the MgO/Fe_2O_3 composites under optimum conditions. Fig. 9a shows a negligible decrease in the RhB concentration in the presence of a light source without the MgO/Fe_2O_3 composites. The maximum RhB degradation rates for S_1, S_2, and S_3 are 98.41%, 98.67%, and 98.23%, respectively, after a reaction time of 150 min (Fig. 11a). The results show the coordination curves of RhB concentration as a function of photocatalytic time. According to the fitting curves, $\ln(C_0/C)$ is linearly correlated with the photocatalytic time. The regression coefficients (R^2) of the fitted lines for S_1, S_2, and S_3 are 0.99803, 0.99180, and 0.98907, respectively (Fig. 11b). This confirms that the composite-mediated photocatalytic RhB degradation followed pseudo-first-order kinetics:

$$\ln\left(\frac{C_0}{C}\right) = Kt \tag{4}$$

where C, C_0, and K represent the RhB content at time t, the original RhB content, and the reaction rate constant, respectively. The rate constant, time required to degrade 50% of the initial RhB concentration (half-life), and R^2 were calculated from the kinetic plots. The rate constants for S_1, S_2, and S_3 were 0.02919, 0.02769, and 0.02813 min^{-1}, respectively. The kinetic constant of the control test without composites was 0.00011166 min^{-1}. The rate constants indicated that the degradation performance of the test with the synthesized samples was higher than that of the control test without the composites.

3.11. Effect of H_2O_2 amount on RhB degradation

The effects of 50, 100, and 200 μL H_2O_2 and the catalyst (MgO/Fe_2O_3) on catalytic RhB degradation under solar irradiation were also investigated. H_2O_2 is one of the most common electron acceptors that improves the photocatalytic process by increasing •OH production in the environment [45]. When introduced into the solution, it competes with other species to capture electrons; however, it is more likely to capture electrons because it is a strong oxidizing agent. Thus, electron–hole recombination is reduced, and the process efficiency increases. H_2O_2 was added to the photocatalytic reactor at three different concentrations under the optimum conditions to investigate its effects (Fig. 12). H_2O_2 addition increased degradation efficiency and decreased dye removal time. Photocatalytic degradation efficiency after adding 50 and 100 μL H_2O_2 was 100%, while adding 200 μL H_2O_2 removed 96% of the dye after 15 min. The dye-removal efficiency without the addition of H_2O_2 was 98% after 150 min. The results of the control experiments showed that H_2O_2 alone had a negligible impact on the degradation, resulting in less than 5% degradation. According to previous reports, H_2O_2 can be photolyzed [46].

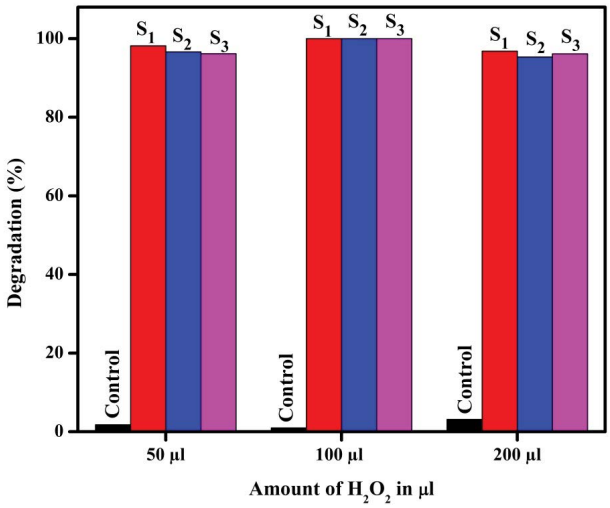

Fig. 12. Different amount of H_2O_2 impact on photocatalytic RhB degradation.

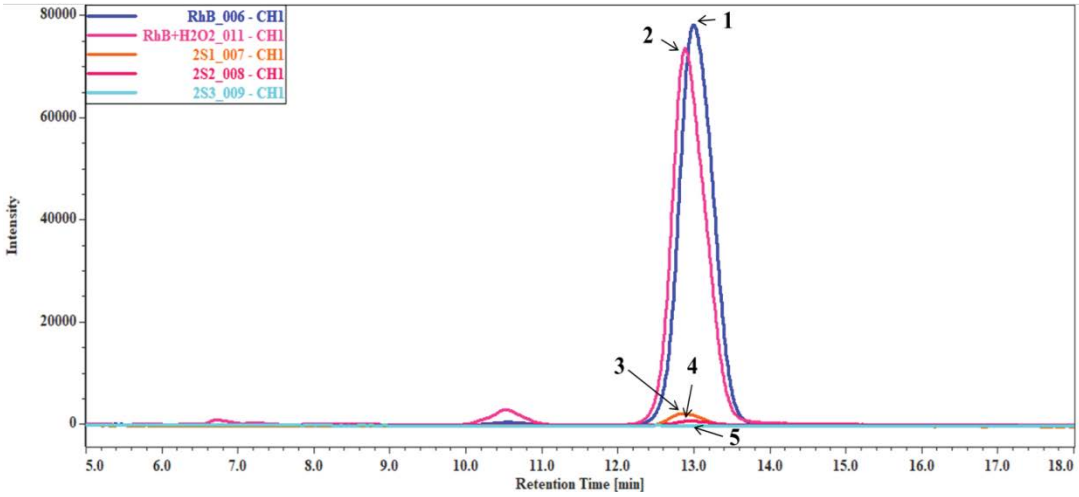

Fig. 13. High-performance liquid chromatogram after irradiating with sunlight for 15 min. (1) Pure RhB, (2) RhB + H_2O_2, (3) RhB + H_2O_2 + sunlight (S_1), (4) RhB + H_2O_2 + sodium light (S_2), and (5) RhB + H_2O_2 + LED light (S_3).

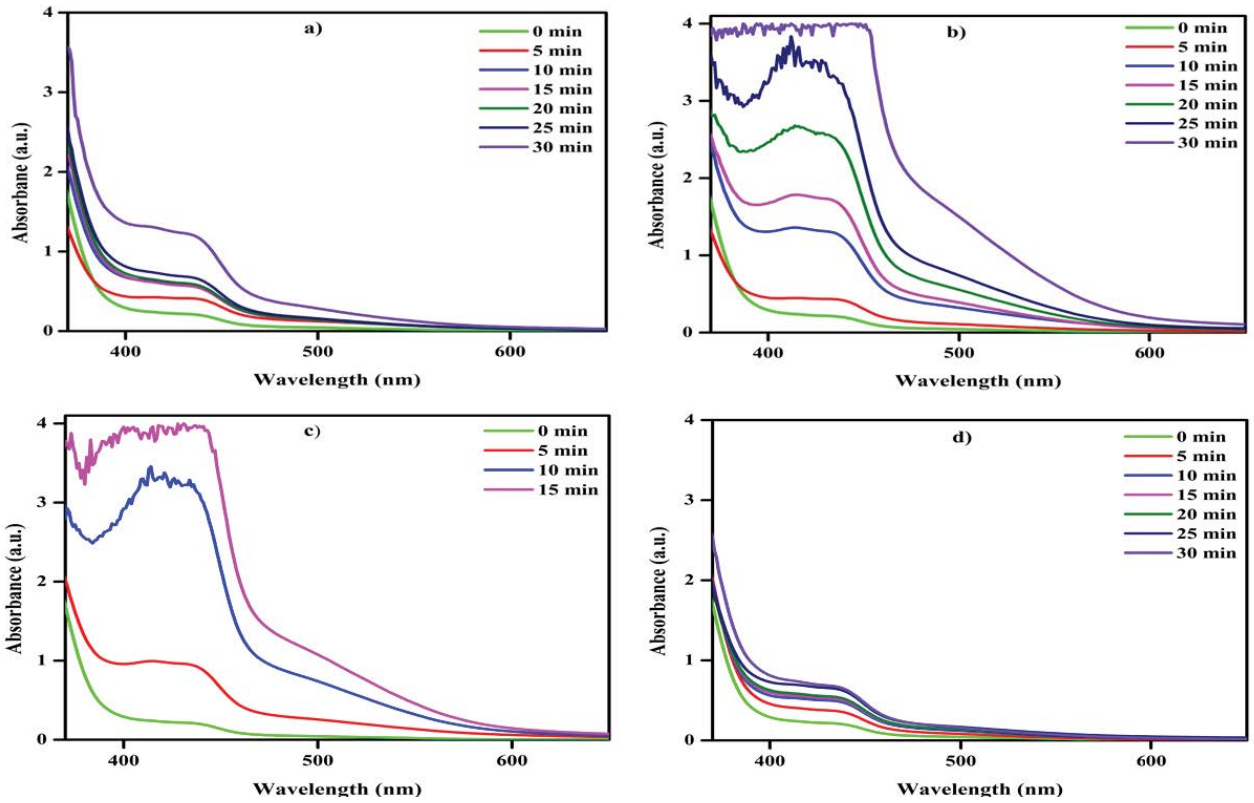

Fig. 14. Absorption peak of 2-aminophenol oxidation product after catalysis with (a) control, (b) sunlight (S_1), (c) sodium lamp (S_2), and (d) LED (S_3) composite catalyst.

$$H_2O_2 + h\nu \rightarrow 2HO^{\bullet} \quad \text{(I)}$$

$$2H_2O_2 + h\nu \rightarrow 2H_2O + O_2 \quad \text{(II)}$$

$$e^- + H_2O_2 \rightarrow OH^{\bullet} + OH^- \quad \text{(III)}$$

$$h^+ + OH^- \rightarrow OH^{\bullet} \quad \text{(IV)}$$

$$e^- + O_2 \rightarrow O_2^- \quad \text{(V)}$$

$$RH + OH^{\bullet} \rightarrow H_2O + R \rightarrow \text{Further oxidation} \quad \text{(VI)}$$

(RH = organic molecules).

The addition of H_2O_2 increased the photodegradation efficiency and time (Fig. 12). However, adding excess H_2O_2 can trap •OH radicals and produce HO_2 radicals, which are weaker oxidizing agents than •OH radicals. Therefore, excess H_2O_2 in the system can reduce photocatalytic degradation efficacy [45].

3.12. HPLC analysis

Photocatalytic degradation was conducted by irradiating 20 ppm RhB, 20 mg composite, and 100 μL H_2O_2 with sunlight for 15 min. After degradation, the samples were analyzed using HPLC, and the results are shown in Fig. 13. The RhB retention time in the control system was 13.02 min, which corresponded to the retention time of the pure dye. The retention time after adding 100 μL H_2O_2 without adding the catalyst in the presence of solar irradiation was 12.9 min. The degradation results show that when the dye was degraded by the composites, new peaks formed after 12.9 min, indicating that the dye was degraded into smaller molecules. Thus, HPLC analysis supported RhB degradation by the MgO/Fe_2O_3 composites (S_1, S_2, and S_3).

3.13. Phenoxazinone synthase-like activities

The activity of MgO/Fe_2O_3 composites were investigated as catalysts for the auto-oxidation of 2-aminophenol to 2-amino-3H-phenoxazine-3-one [47]. Ethanol was selected as the reaction medium to simulate the physiological conditions. The catalytic reactions were evaluated by observing the increase in the characteristic absorption band of the phenoxazinone chromophore at 430 nm as a function of time. Representative spectral growth over time for complex 3 is shown in Fig. 14. The phenoxazinone synthase efficiencies for the control solution (without the catalyst), S_1, S_2, and S_3 were 84%, 94%, 94%, and 68%, respectively, after 30 min (Fig. 14a–d) The phenoxazinone synthase efficiency of S_2 was 94% within 15 min, and a low efficiency was obtained for S_3 (Fig. 14c and d). Overall, S_2 synthesized a large amount of phenoxazinone.

4. Conclusion

The MgO/Fe_2O_3 composites effectively degraded RhB. The optimal reaction conditions were a dye solution of pH 4.0, 20 mg of catalyst, and 100 μL of H_2O_2. Under these conditions, 100% of the 20 ppm RhB solution was degraded within 15 min. The strong oxidation capacity of the MgO/Fe_2O_3 composites/H_2O_2 was mostly due to the action of hydroxyl radicals, which revealed its strong ability to degrade RhB. Based on the control experiments, H_2O_2 alone degraded less than 5% of the RhB. Furthermore, the changes in the peak pattern, absorbance, and HPLC results supported the degradation of RhB by the MgO/Fe_2O_3 composites. Phenoxazinone synthase efficiencies were 94%, 94%, and 68% for S_1, S_2, and S_3, respectively. The efficiency of the control solution (without catalyst) was 84% after 30 min. The results revealed that the MgO/Fe_2O_3 photocatalyst in the presence of H_2O_2 under solar irradiation was the most effective for RhB photodecomposition. In addition, the composites exhibited good phenoxazinone synthase activity. MgO/Fe_2O_3 composites are expected to be applicable in the industrial wastewater remediation and pharmaceutical fields in the near future.

Acknowledgement

This work was supported by a 2-Year Research Grant of Pusan National University.

References

[1] R.L. Kadam, Y. Kim, S. Gailkwad, M. Chang, N.H. Tarte, S. Han, Catalytic decolorization of Rhodamine B, Congo red, and Crystal violet dyes, with a novel niobium oxide anchored molybdenum (Nb–O–Mo), Catalysts, 10 (2020) 1–17.
[2] H. Du, Y. Zhang, H. Jiang, H. Wang, Adsorption of Rhodamine B on polyvinyl chloride, polystyrene, and polyethylene terephthalate microplastics in aqueous environments, Environ. Technol. Innovation, 27 (2022) 102495, doi: 10.1016/j.eti.2022.102495.
[3] M. Kumar, S. Changan, M. Tomar, U. Prajapati, V. Saurabh, M. Hasan, M. Sasi, C. Maheshwari, S. Singh, S. Dhumal, Radha, M. Thakur, S. Punia, V. Satankar, R. Amarowicz, M. Mekhemar, Custard apple (*Annona squamosa* L.) leaves: nutritional composition, phytochemical profile, and health-promoting biological activities, Biomolecules, 11 (2021) 614, doi: 10.3390/biom11050614.
[4] R.A. Nasr, E.A.B. Ali, Polyethersulfone/gelatin nano-membranes for the Rhodamine B dye removal and textile industry effluents treatment under cost effective condition, J. Environ. Chem. Eng., 10 (2022) 107250, doi: 10.1016/j.jece.2022.107250.
[5] X. Wang, X. Feng, J. Shang, Efficient photoelectrochemical oxidation of Rhodamine B on metal electrodes without photocatalyst or supporting electrolyte, Front. Environ. Sci. Eng., 12 (2018) 11, doi: 10.1007/s11783-018-1061-8.
[6] A.I. Adeogun, R.B. Balakrishnan, Kinetics, isothermal and thermodynamics studies of electrocoagulation removal of basic dye Rhodamine B from aqueous solution using steel electrodes, Appl. Water Sci., 7 (2017) 1711–1723.
[7] B. Cuiping, X. Xianfeng, G. Wenqi, F. Dexin, X. Mo, G. Zhongxue, X. Nian, Removal of Rhodamine B by ozone-based advanced oxidation process, Desalination, 278 (2011) 84–90.
[8] P. Gayathri, R. Praveena Juliya Dorathi, K. Palanivelu, Sonochemical degradation of textile dyes in aqueous solution using sulphate radicals activated by immobilized cobalt ions, Ultrason. Sonochem., 17 (2010) 566–571.
[9] J. Mishra, R. Saini, D. Singh, Review paper on removal of heavy metal ions from industrial waste water effluent, IOP Conf. Ser.: Mater. Sci. Eng., 1168 (2021) 012027, doi: 10.1088/1757-899X/1168/1/012027.
[10] I. Sirés, E. Brillas, M.A. Oturan, M.A. Rodrigo, M. Panizza, Electrochemical advanced oxidation processes: today and tomorrow. A review, Environ. Sci. Pollut. Res., 21 (2014) 8336–8367.
[11] S. Akter, M.B.K. Suhan, M.S. Islam, Recent advances and perspective of electrocoagulation in the treatment of wastewater: a review, Environ. Nanotechnol. Monit. Manage., 17 (2022) 100643, doi: 10.1016/j.enmm.2022.100643.
[12] S. Rizvi, A. Singh, A. Kushwaha, S.K. Gupta, Chapter 16 – Recent Advances in Melanoidin Removal from Wastewater: Sources, Properties, Toxicity, and Remediation Strategies, C.M. Hussain, S. Singh, L. Goswami, Eds., Emerging Trends to Approaching Zero Waste: Environmental and Social Perspectives, Elsevier, 2021, pp. 361–386.
[13] E.M. Cuerda-Correa, M.F. Alexandre-Franco, C. Fernández-González, Advanced oxidation processes for the removal of antibiotics from water. An overview, Water, 12 (2020) 102, doi: 10.3390/w12010102.
[14] E.A. Serna-Galvis, J. Porras, R.A. Torres-Palma, A critical review on the sonochemical degradation of organic pollutants in urine, seawater, and mineral water, Ultrason. Sonochem., 82 (2022) 105861, doi: 10.1016/j.ultsonch.2021.105861.

[15] K. Ravichandran, D.S. Vasanthi, P. Kavitha, R. Shalini, S. Suvathi, P.K. Praseetha, Cost-effective and eco-friendly dye degradation by enzyme-powered ZnO nanomaterial: effect of process temperature, Bull. Mater. Sci., 45 (2022) 40, doi: 10.1007/s12034-021-02619-8.
[16] Z.A. Mahar, G.Q. Shar, A. Balouch, A.H. Pato, A.R. Shaikh, Effective and viable photocatalytic degradation of Rhodamine B dye in aqueous media using CuO/PVA nanocomposites, New J. Chem., 45 (2021) 16500–16510.
[17] P.S. Chauhan, K. Kumar, K. Singh, S. Bhattacharya, Fast decolorization of Rhodamine B dye using novel V_2O_5-rGO photocatalyst under solar irradiation, Synth. Met., 283 (2022) 116981, doi: 10.1016/j.synthmet.2021.116981.
[18] T. Amakali, A. Živković, M.E.A. Warwick, D.R. Jones, C.W. Dunnill, L.S. Daniel, V. Uahengo, C.E. Mitchell, N.Y. Dzade, N.H. de Leeuw, Photocatalytic degradation of Rhodamine B dye and hydrogen evolution by hydrothermally synthesized $NaBH_4$—spiked ZnS nanostructures, Front. Chem., 10 (2022) 835832, doi: 10.3389/fchem.2022.835832.
[19] H. Ashiq, N. Nadeem, A. Mansha, J. Iqbal, M. Yaseen, M. Zahid, I. Shahid, G-C_3N_4/Ag@$CoWO_4$: a novel sunlight active ternary nanocomposite for potential photocatalytic degradation of Rhodamine B dye, J. Phys. Chem. Solids, 161 (2022) 110437, doi: 10.1016/j.jpcs.2021.110437.
[20] J. Sandhya, S. Kalaiselvam, UV responsive quercetin derived and functionalized CuO/ZnO nanocomposite in ameliorating photocatalytic degradation of Rhodamine B dye and enhanced biocidal activity against selected pathogenic strains, J. Environ. Sci. Health. Part A Toxic/Hazard. Subst. Environ. Eng., 56 (2021) 835–848.
[21] S. Zhao, C. Chen, J. Ding, S. Yang, Y. Zang, N. Ren, One-pot hydrothermal fabrication of $BiVO_4$/Fe_3O_4/rGO composite photocatalyst for the simulated solar light-driven degradation of Rhodamine B, Front. Environ. Sci. Eng., 16 (2022) 36, doi: 10.1007/s11783-021-1470-y.
[22] M.S.H. Bhuiyan, M.Y. Miah, S.C. Paul, T. Das Aka, O. Saha, M.M. Rahaman, M.J.I. Sharif, O. Habiba, M. Ashaduzzaman, Green synthesis of iron oxide nanoparticle using *Carica papaya* leaf extract: application for photocatalytic degradation of Remazol Yellow RR dye and antibacterial activity, Heliyon, 6 (2020) e04603, doi: 10.1016/j.heliyon.2020.e04603.
[23] A. Fouda, S.E.D. Hassan, E. Saied, M.F. Hamza, Photocatalytic degradation of real textile and tannery effluent using biosynthesized magnesium oxide nanoparticles (MgO-NPs), heavy metal adsorption, phytotoxicity, and antimicrobial activity, J. Environ. Chem. Eng., 9 (2021) 105346, doi: 10.1016/j.jece.2021.105346.
[24] N. Kumari, S. Prakash, M. Kumar, Radha, B. Zhang, V. Sheri, N. Rais, D. Chandran, A. Dey, T. Sarkar, S. Dhumal, S. Kumar, D.K. Mahato, M. Vishvanathan, P. Mohankumar, M. Pateiro, J.M. Lorenzo, Seed waste from Custard apple (*Annona squamosa* L.): a comprehensive insight on bioactive compounds, Processes, 10 (2022) 2119, doi: 10.3390/pr10102119.
[25] N. Zada, K. Saeed, I. Khan, Decolorization of Rhodamine B dye by using multiwalled carbon nanotubes/Co–Ti oxides nanocomposite and Co–Ti oxides as photocatalysts, Appl. Water Sci., 10 (2020) 40, doi: 10.1007/s13201-019-1124-4.
[26] J. Wu, W. Liu, R. Zhu, X. Zhu, On-line separation/analysis of Rhodamine B dye based on a solid-phase extraction high performance liquid chromatography self-designed device, RSC Adv., 11 (2021) 8255–8263.
[27] G. Balakrishnan, R. Velavan, K. Mujasam Batoo, E.H. Raslan, Microstructure, optical and photocatalytic properties of MgO nanoparticles, Results Phys., 16 (2020) 103013, doi: 10.1016/j.rinp.2020.103013.
[28] L. Balan, C. Matei Ghimbeu, L. Vidal, C. Vix-Guterl, Photoassisted synthesis of manganese oxide nanostructures using visible light at room temperature, Green Chem., 15 (2013) 2191–2199.
[29] A.V. Ramesh, D. Rama Devi, S. Mohan Botsa, K. Basavaiah, Facile green synthesis of Fe_3O_4 nanoparticles using aqueous leaf extract of *Zanthoxylum armatum* DC. for efficient adsorption of methylene blue, J. Asian Ceram. Soc., 6 (2018) 145–155.
[30] F. Alakhras, E. Alhajri, R. Haounati, H. Ouachtak, A.A. Addi, T.A. Saleh, A comparative study of photocatalytic degradation of Rhodamine B using natural-based zeolite composites, Surf. Interfaces, 20 (2020) 100611, doi: 10.1016/j.surfin.2020.100611.
[31] G. Sathishkumar, V. Logeshwaran, S. Sarathbabu, P.K. Jha, M. Jeyaraj, C. Rajkuberan, N. Senthilkumar, S. Sivaramakrishnan, Green synthesis of magnetic Fe_3O_4 nanoparticles using *Couroupita guianensis* Aubl. fruit extract for their antibacterial and cytotoxicity activities, Artif. Cells Nanomed. Biotechnol., 46 (2018) 589–598.
[32] P.K. Dhar, P. Saha, M.K. Hasan, M.K. Amin, M.R. Haque, Green synthesis of magnetite nanoparticles using *Lathyrus sativus* peel extract and evaluation of their catalytic activity, Cleaner Eng. Technol., 3 (2021) 100117, doi: 10.1016/j.clet.2021.100117.
[33] J. Pathak, Identification of phytochemicals from seed extract of Custard Apple (*Annona squamosa* L.), Biosci. Biotechnol. Res. Commun., 14 (2021) 397–402.
[34] E.M. Mostafa, E. Amdeha, Enhanced photocatalytic degradation of malachite green dye by highly stable visible-light-responsive Fe-based tri-composite photocatalysts, Environ. Sci. Pollut. Res., 29 (2022) 69861–69874.
[35] A. Venkatachalam, J.P. Jesuraj, K. Sivaperuman, *Moringa oleifera* leaf extract-mediated green synthesis of nanostructured alkaline earth oxide (MgO) and its physicochemical properties, J. Chem., 2021 (2021) 4301504, doi: 10.1155/2021/4301504.
[36] S. Sebatini, S. Kalluri, A. Anish Madhavan, Green synthesized α-Fe_2O_3 mesoporous network for heterogeneous Fenton oxidation of thiazine dye, Mater. Lett.: X, 5 (2020) 100037, doi: 10.1016/j.mlblux.2019.100037.
[37] M.A. Elobeid, M.A. Awad, P. Virk, K.M. Ortashi, N.M. Merghani, A.M. Asiri, E.A.A. Bashir, Synthesis and characterization of noble metal/metal oxide nanoparticles and their potential antidiabetic effect on biochemical parameters and wound healing, Green Process Synth., 11 (2022) 106–115.
[38] P.K. Palai, A. Mondal, C.K. Chakraborti, I. Banerjee, K. Pal, V.S.S. Rathnam, Doxorubicin loaded green synthesized nano-ceria decorated functionalized graphene nanocomposite for cancer-Specific drug release, J. Cluster Sci., 30 (2019) 1565–1582.
[39] S. Prashanna Suvaitha, T. Divya, P. Sridhar, P. Palani, K. Venkatachalam, Optical and biological properties of MgO/ZnO nanocomposite derived via eggshell membrane: a bio-waste approach, Bioprocess Biosyst. Eng., 46 (2023) 39–51.
[40] D.A. Demirezen, Ş. Yılmaz, D.D. Yılmaz, Y.Ş. Yıldız, Green synthesis of iron oxide nanoparticles using *Ceratonia siliqua* L. aqueous extract: improvement of colloidal stability by optimizing synthesis parameters, and evaluation of antibacterial activity against gram-positive and gram-negative bacteria, Int. J. Mater. Res., 113 (2022) 849–861.
[41] R. Periakaruppan, V. Naveen, J. Danaraj, Green synthesis of magnesium oxide nanoparticles with antioxidant potential using the leaf extract of *Piper nigrum*, JOM, 74 (2022) 4817–4822.
[42] G. Sharma, D.D. Dionysiou, S. Sharma, A. Kumar, A.H. Al-Muhtaseb, M. Naushad, F.J. Stadler, Highly efficient Sr/Ce/activated carbon bimetallic nanocomposite for photonduced degradation of Rhodamine B, Catal. Today, 335 (2019) 437–451.
[43] K.M. Reza, A. Kurny, F. Gulshan, Parameters affecting the photocatalytic degradation of dyes using TiO_2: a review, Appl. Water Sci., 7 (2017) 1569–1578.
[44] K. Byrappa, A.K. Subramani, S. Ananda, K.M. Lokanatha Rai, R. Dinesh, M. Yoshimura, Photocatalytic degradation of Rhodamine B dye using hydrothermally synthesized ZnO, Bull. Mater. Sci., 29 (2006) 433–438.
[45] R. Rahmati, B. Nayebi, B. Ayati, Investigating the effect of hydrogen peroxide as an electron acceptor in increasing the capability of slurry photocatalytic process in dye removal, Water Sci. Technol., 83 (2021) 2414–2423.
[46] D. Saha, M.M. Desipio, T.J. Hoinkis, E.J. Smeltz, R. Thorpe, D.K. Hensley, S.G. Fischer-Drowos, J. Chen, Influence of hydrogen peroxide in enhancing photocatalytic activity of carbon nitride under visible light: an insight into reaction intermediates, J. Environ. Chem. Eng., 6 (2018) 4927–4936.
[47] M. Palaniappan, D. Selvaraj, S. Kandasamy, Y.H. Kahng, M. Narayanan, R. Rajendran, R. Rangappan, Architectural MCM 41 was anchored to the Schiff base Co(II) complex to enhance methylene blue dye degradation and mimic activity, Environ. Res., 215 (2022) 114325, doi: 10.1016/j.envres.2022.114325.